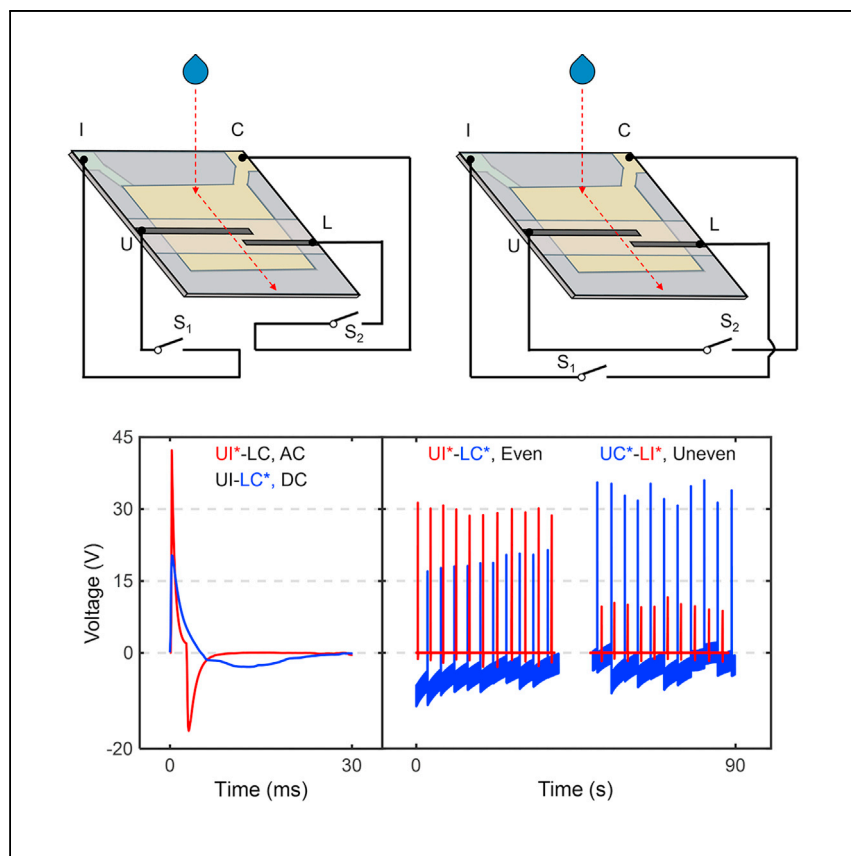


Article

A four-electrode droplet triboelectric nanogenerator providing multimodal output



He et al. report a droplet triboelectric nanogenerator with four electrodes (FED-TENG), and it could provide pseudo direct current output, alternating current output, evenly distributed dual output, and unevenly distributed dual output. Compared to the reported water-TENG, FED-TENG shows enhanced flexibility and adaptability.

Peng He, Jing Ding, Le Lei,
Wen-Quan Tao

wqtao@mail.xjtu.edu.cn

Highlights

Four-electrode droplet triboelectric nanogenerator enables multimodal outputs

DC or AC output can be selectively generated

Dual outputs with evenly or unevenly distributed power are available

Multimodal mechanism is elucidated by capacitor charging/discharging



Article

A four-electrode droplet triboelectric nanogenerator providing multimodal output

Peng He,^{1,3} Jing Ding,^{2,3} Le Lei,¹ and Wen-Quan Tao^{1,4,*}

SUMMARY

Water-triboelectric nanogenerators, leveraging contact electrification between water and solid surfaces, have exhibited significant potential to harvest energy. Different configurations of triboelectric nanogenerators offer various functionalities and promising application scenarios. This study introduces a four-electrode droplet triboelectric nanogenerator (FED-TENG). Different connection formats among the four electrodes result in multimodal outputs, enhancing adaptability across diverse applications. The selective generation of direct current (DC) and alternating current (AC) output enables efficient, direct driving of DC or AC loads. The device also offers dual outputs distributed evenly or unevenly in power. Evenly distributed dual output accommodates simultaneous power supply to multiple similar loads, while unevenly distributed dual output is recommended for independent sensor applications. Additionally, the charge-transfer process in FED-TENG is dissected to elucidate the mechanism underlying different output modes. Anticipated findings from investigating FED-TENG hold promise for developing adaptable and versatile water-TENGs applicable to droplet energy-harvesting and sensor technologies.

INTRODUCTION

Utilization of traditional energy, primarily fossil fuels, has resulted in many environmental problems, notably contributing to global warming and pollution. Consequently, extensive research has been dedicated to the exploration of green-energy alternatives. Among various forms of clean, renewable energy, hydraulic energy has found widespread applications through hydroelectric stations that harness the potential energy of river water. Beyond hydraulic energy, various natural movements of water widely observed in nature, such as raindrops, ocean waves, and tides, present opportunities for generating electricity.¹ The emergence of Internet of Things, artificial intelligence, and wireless sensor networks, reliant on mobile and wireless power sources, has spurred technological advancements to harness dispersed energy sources. Initially devised to harvest energy from contact electrification between solid and solid,^{2–7} triboelectric nanogenerators (TENGs) have undergone further development to scavenge diverse forms of water-based energy by exploiting the contact electrification between liquid and solid,^{1,8–33} introducing a new category of TENG known as water-TENG. This paper will specifically focus on water-TENGs designed to harvest energy from water droplets.

A large variety of water-TENGs have been extensively studied, with the predominant electrode configurations encompassing a single electrode^{13–37} and double electrodes.^{38–47} These electrode configurations in water-TENGs could act as either a sensor or an energy-harvesting device. In comparison with the alternating current

¹Key Laboratory of Thermo-Fluid Science and Engineering, Ministry of Education, School of Energy & Power Engineering, Xi'an Jiaotong University, Shaanxi 710049, China

²Department of Mechanical and Nuclear Engineering, Kansas State University, Manhattan, KS 66506, USA

³These authors contributed equally

⁴Lead contact

*Correspondence: wqtao@mail.xjtu.edu.cn
<https://doi.org/10.1016/j.xcrp.2024.101800>



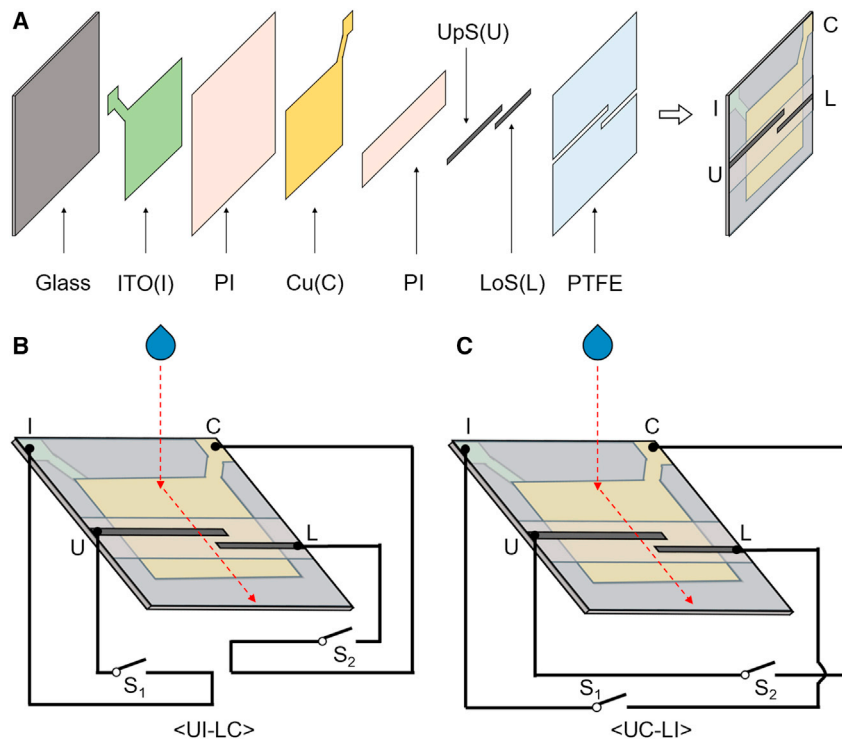


Figure 1. Structure and circuit diagram of FED-TENG

(A) Schematic illustration of FED-TENG.

(B and C) Circuit diagrams of <UI-LC> series (B) and <UC-LI> series (C).

Legend: : glass; : ITO; : PI; : Cu; : PTFE; : steel; and : droplet.

(AC) output of solid-solid TENGs, water-TENGs employing single or double electrodes typically produce AC output characterized by distinct, sharp peaks and subtle, gradual troughs,^{1,37–39} termed pseudo direct current (PDC). The efficiency of water-TENGs tends to diminish when generating AC output due to the less efficient conversion from DC to AC compared with the reverse process in solid-solid TENGs. Therefore, the development of water-TENGs capable of generating AC output is crucial for expanding their potential applications. Many reported water-TENGs with single or double electrodes could power electronic devices.^{18,22,23,37,41} However, using a water-TENG solely as a sensor,^{12,48} despite its lower power output, is deemed inefficient. To optimize efficiency, particularly as sensors often necessitate auxiliary circuits, a more pragmatic approach involves dividing the output into two parts. The minor portion serves as the sensor signal, while the major portion powers auxiliary circuits. Incorporating dual outputs within a water-TENG stands as a promising strategy to facilitate this division of electric output.

To address the identified technological gaps within water-TENGs, this paper introduces a four-electrode droplet TENG (FED-TENG). Employing diverse configurations of the four electrodes, FED-TENG presents multimodal outputs, encompassing PDC output, AC output, evenly distributed dual output, and unevenly distributed dual output. Additionally, a detailed analysis of the charge-transfer process is conducted to elucidate the underlying mechanisms governing the various output modes. In direct comparison with the prevailing state-of-the-art water-TENG, FED-TENG shows enhanced flexibility and adaptability.

RESULTS AND DISCUSSION

Characterization

Adopting the double-electrode configuration proposed by Xu et al.,³⁸ FED-TENG was devised (Figure 1). Four electrodes were interwoven to create two pairs of output ports. The composition of FED-TENG, arranged from bottom to top (left to right in Figure 1A), comprised glass, indium tin oxide (ITO), polyimide (PI), copper (Cu), another layer of PI, two steel pieces, and polytetrafluoroethylene (PTFE). Glass was selected as the substrate material, while PI served as electrical insulation. The ITO and Cu films functioned as an ITO electrode (ITOE) and a Cu electrode (CuE), respectively. Steel and ITO are chosen because they are accessible materials in the lab. Xu et al.³⁸ had shown that the strip electrode does not influence the output of the TENG. In practical use, a kind of material that is hard to erode will be chosen. To prevent the film electrodes from contacting any remaining water along the edges, their dimensions were reduced by 5 mm in both length and width compared to the substrate. PTFE was employed as the triboelectrification material. Two steel pieces were utilized as an upper steel electrode (UpSE) and a lower steel electrode (LoSE). The PTFE film had an average thickness of approximately 6.35 μm , and its surface exhibited unevenness (Figure S1A), with a maximum peak-to-valley height of around 2.1 μm . Contact-angle measurements indicate that the PTFE film had a contact angle of 117.72°, while the steel electrodes exhibited a contact angle of 100.11° (Figure S1B). Both the PTFE film and steel electrodes had contact angles exceeding 100°, ensuring smooth movement of droplets across the device.

Compared with single- and double-electrode water-TENGs, the incorporation of additional electrodes in FED-TENG facilitates the provision of various output modes. In Figures 1B and 1C, two series of modes, denoted as <UI-LC> and <UC-LI>, are presented, wherein U, L, I, and C represent UpSE, LoSE, ITOE, and CuE, respectively. Within the <UI-LC> series, closing either switch S_1 or S_2 leads to the output mode UI or LC. When a measuring instrument is introduced into the circuit, these modes are labeled as UI* and LC*, with the asterisk indicating the measured port. Simultaneous closure of both switches yields the UI-LC output mode. Notably, the UI-LC mode encompasses two output ports (UI and LC), further categorized as UI*-LC, UI-LC*, and UI*-LC*, contingent upon the port measured. Consequently, the <UI-LC> series encompasses five output modes: UI*, LC*, UI*-LC, UI-LC*, and UI*-LC*. Similarly, the <UC-LI> series includes UC*, LI*, UC*-LI, UC-LI*, and UC*-LI* modes. In total, 10 output modes were characterized in this study. Modes such as UI*, LC*, LI*, and UC* are termed singly connected modes, while their parallelly connected counterparts, including UI*-LC, UI-LC*, UC*-LI, and UC-LI*, present a single output. Additionally, UI*-LC* and UC*-LI* provide dual output. A summary detailing the switch state and measured port for each mode is presented in Table 1. In ideal condition, an ammeter possesses an internal resistance of zero, while a voltmeter exhibited an infinite internal resistance. During the measurement of short-circuit current in UI*-LC, UI-LC*, and UI*-LC* modes, these modes are equivalent. Similarly, the UC*-LI, UC-LI*, and UC*-LI* modes are equivalent under the same conditions. For the measurement of open-circuit voltage, the UI* mode is equivalent to UI*-LC*, and the LC* is equivalent to the UI*-LC* mode. Similarly, the UC* mode is equivalent to the UC*-LI* mode, and the LI* mode is equivalent to the UC*-LI* mode under the same conditions.

Polarity

In Figures 2A and S2, FED-TENG was inclined at a 45° angle to the horizontal plane, and 100- μL tap water droplets were released sequentially from a 15-cm height

Table 1. Switch state and output modes

Series	Mode	Switch state	Measured port	Equivalent modes for current measurement	Equivalent modes for voltage measurement
<UI-LC>	UI*	Figure 1B; S ₁ is on, S ₂ is off.	UI	–	UI*-LC*
	UI*-LC	Figure 1B; S ₁ is on, S ₂ is on.	UI	UI-LC*, UI*-LC*	–
	LC*	Figure 1B; S ₁ is off, S ₂ is on.	LC	–	UI*-LC*
	UI-LC*	Figure 1B; S ₁ is on, S ₂ is on.	LC	UI*-LC, UI*-LC*	–
	UI*-LC*	Figure 1B; S ₁ is on, S ₂ is on.	UI and LC	UI-LC*, UI*-LC	UI*, LC*
<UC-LI>	UC*	Figure 1C; S ₁ is off, S ₂ is on.	UC	–	UC*-LI*
	UC*-LI	Figure 1C; S ₁ is on, S ₂ is on.	UC	UC-LI*, UC*-LI*	–
	LI*	Figure 1C; S ₁ is on, S ₂ is off.	LI	–	UC*-LI*
	UC-LI*	Figure 1C; S ₁ is on, S ₂ is on.	LI	UC*-LI, UC*-LI*	–
	UC*-LI*	Figure 1C; S ₁ is on, S ₂ is on.	UC and LI	UC*-LI, UC-LI*	UC*, LI*

above the PTFE surface. The selection of the inclination angle, droplet size, and dropping height in this study aligns with common and typical parameters in droplet-TENG research. During experimentation, the electric output was recorded as the droplets impinged on and slid off the surface. Before measurement, PTFE film was charged by the dripping droplets. Following the impingement of 2,500 droplets, the open-circuit voltage between the ITOE and UpSE reached a plateau (Figure 2B), indicating the full charging of the PTFE.

Similar to the double-electrode water-TENG, the functionality of the FED-TENG is confined to specific regions on the PTFE surface. During the experiment, droplets were directed to impinge either on the left side (Figure 2C) or the right side (Figure 2D) of the device. In both figures, the blue dash-line circle signifies the moment of droplet contact or departure from UpSE, while the yellow dash line denotes the moment of droplet contact or departure from LoSE. The red point marks the contact

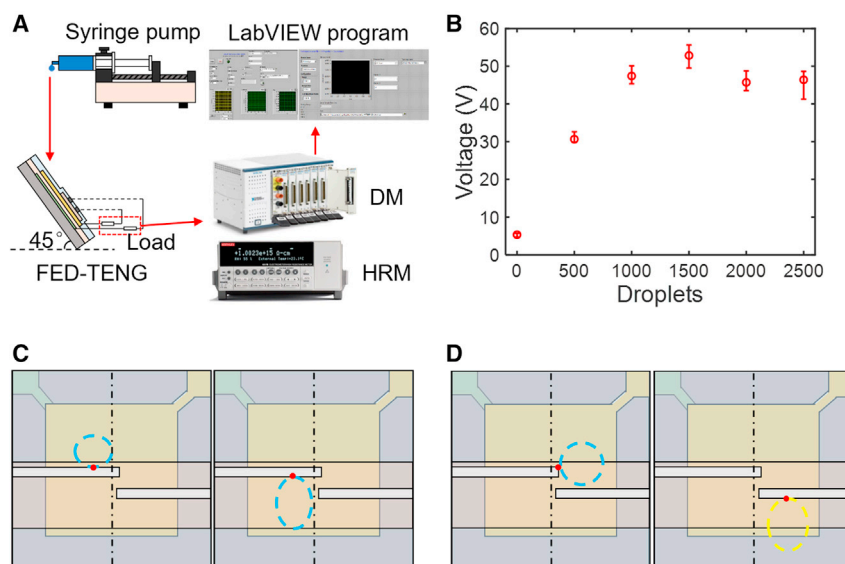


Figure 2. Electric output measurement of FED-TENG

(A) Schematic of electric output measurement system. DM stands for digital multimeter, and HRM is the abbreviation for high-resistance meter.

(B) Open-circuit voltage of UI* when PTFE was being charged. Error bars are the standard deviations for more than ten measurements of each point.

(C and D) Schematic diagrams of a droplet impinging on the left side (C) and the right side (D).

point. When a droplet impinges on the left side, it contacts UpSE first and leaves UpSE last, whereas when impinging on right side, it contacts UpSE first and leaves LoSE last. The impinging and sliding processes are detailed in [Figure S3](#). Upon impingement on the left, the timing for contacting UpSE (blue dash line), contacting LoSE (yellow dash line), leaving LoSE (yellow dash line), and leaving UpSE (blue dash line) are 0, 2.86, 22.14, and 25 ms, respectively. Upon impingement on the right, the timings for contacting UpSE (blue circle), contacting LoSE (yellow circle), leaving UpSE (blue line), and leaving LoSE (yellow line) are 0, 1.43, 23.57, and 36.43 ms, respectively. The two maximum spreading areas are observed to be 2.37 cm² (on the left, at 6.43 ms) and 2.35 cm² (on the right, at 7.16 ms), respectively.

For clarity, only the positive (red circles) and negative (black circles) peak values of the short-circuit current and open-circuit voltage are depicted in [Figures 3A–3D](#), while the maximum quantity of transferred charge is detailed in [Figures 3E and 3F](#). With the exception of UI*-LC and UC-LI*, all other modes exhibited significant positive output but negligible negative output, categorized as PDC output. Notably, UI*-LC demonstrated prominent and comparable positive and negative outputs, showcasing AC output rarely observed in existing water-TENGs. Conversely, UC-LI* generated only weak outputs. Interestingly, UI* yielded PDC output, while its parallelly connected counterpart, UI*-LC, generated AC output. [Figure S4](#) presents the outputs of a FED-TENG with a Cu film in place of an ITO film. The outputs were higher compared to those of the FED-TENG employing an ITOE and a CuE, although the waveforms exhibited no difference. The different materials could provide similar output current and voltage despite the amplitude with a gap. However, this research primarily focuses on elucidating the multiple output and mechanism of the FED-TENG rather than optimizing its performance; hence, there is limited analysis regarding the FED-TENG with two Cu film electrodes.

The PDC output of UI* and the AC output of UI*-LC were analyzed across a broad range of load resistance. As the load resistance increased from 10 to 10⁹ Ω, the output voltage consistently rose, with instantaneous power peaking at 10⁵ Ω ([Figures 3G and 3H](#)). Notably, UI* yielded a peak power (*P*) of 2.30 mW, nearly equivalent to the combined positive *P* (+*P*; 1.87 mW) and negative *P* (−*P*; 0.4 mW) of UI*-LC. In essence, compared to UI*, UI*-LC efficiently divided the output power into two opposing phases. This capability allows the FED-TENG to directly power PDC or AC loads without necessitating a power converter, thereby mitigating energy conversion loss and enhancing energy utilization efficiency. It is to be noted that the output of the FED-TENG with two Cu film electrodes is higher than that of the FED-TENG with an ITO film electrode and a Cu film electrode, indicating that the electrode components have an impact on the outputs of such a four-electrode generator. In addition, the output power of 2.3 mW is not optimal, so no comparability with other water-TENGs is conducted.

The electric outputs corresponding to the two droplet-impinging positions are depicted in [Figures 4 and S5](#), and the transferred charges are outlined in [Figure S6](#). The electric outputs of singly connected modes (UI*, LC*, LI*, and UC*) were independent of the two droplet-impinging positions ([Figures S5A–S5H](#)). These modes displayed no charge transfer between the disconnected electrodes during droplet impingement, allowing the disregarding of the disconnected electrodes to simplify the FED-TENG to double-electrode water-TENGs. Similarly, the electric output of the parallelly connected mode UC*-LI was not notably affected by the two droplet-impinging positions ([Figures S5I and S5J](#)). In contrast, other parallelly connected modes such as UI-LC*, UC-LI*, and UI*-LC, exhibited variation with changes

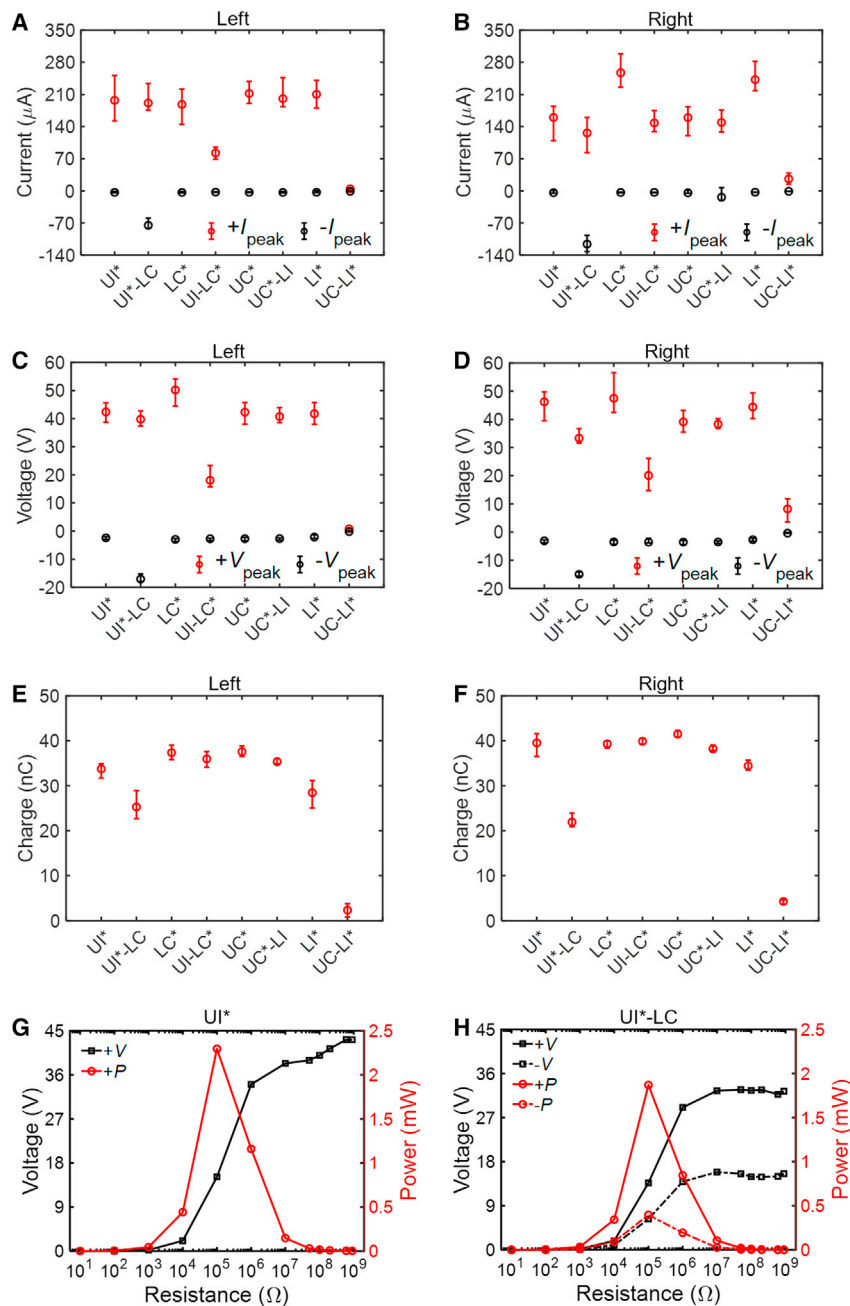


Figure 3. Electric output measurement results of different modes of FED-TENG

(A and B) Peak values of short-circuit current impinging on the left side (A) and on the right side (B). (C and D) Peak values of open-circuit voltage impinging on the left side (C) and on the right side (D). (E and F) Charge transferred when droplets impinge on the left side (E) and on the right side (F). (G) Peak values of open-circuit voltage and power of UI* (G) or UI*-LC (H). Error bars are the standard deviations for more than ten measurements of each point.

in droplet-impinging position (Figure 4). Specifically, UI-LC* and UC-LI* produced lower electric output when droplets were impinged on the left side (Figures 4A–4D). Concerning UI*-LC, while the peak values of the electric output were not prominently impacted by the two droplet-impinging positions, substantial waveform disparities were observed between the left and right cases.

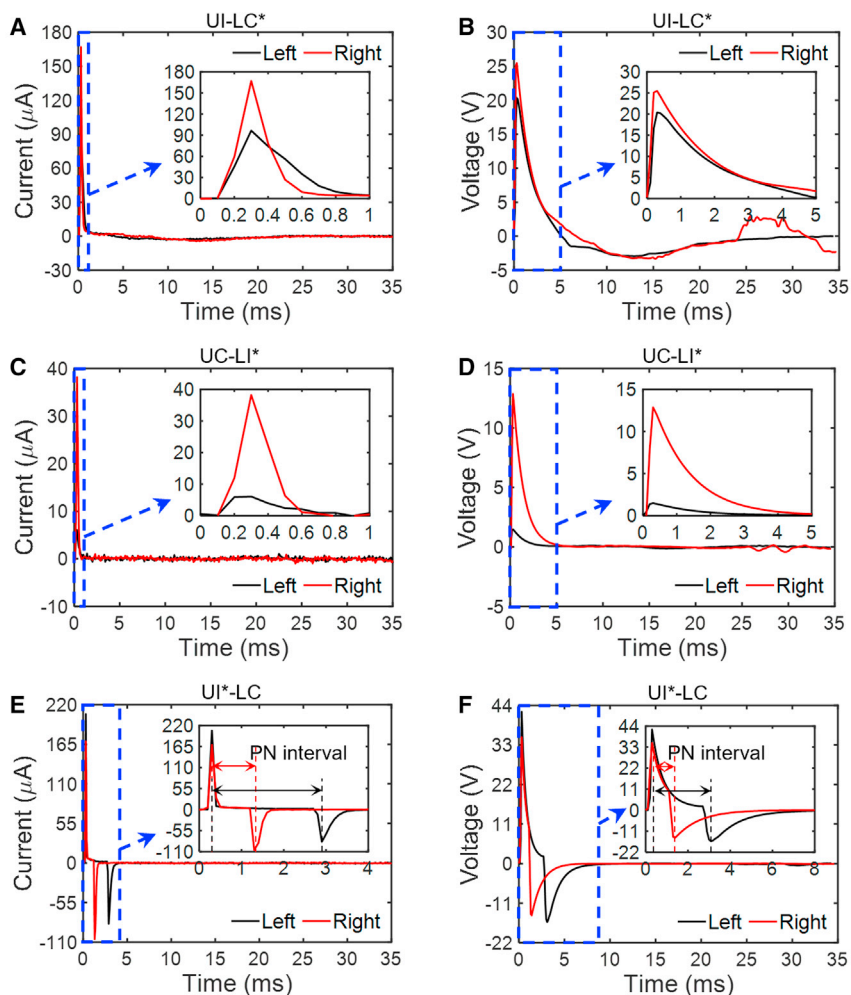


Figure 4. The electric outputs of FED-TENG when the droplet impinges on the two positions (A, C, and E) Short-circuit current of UI-LC* (A), UC-LI* (C), and UI*-LC (E). (B, D, and F) Open-circuit voltage of UI-LC* (B), UC-LI* (D), and UI*-LC (F).

Given that UI*-LC generated AC output, both positive and negative peaks were evident in the output waveforms (Figures 4E and 4F). The interval between these peaks, termed the PN interval henceforth, was notably shorter when droplets impinged on the right side (1.05 ms) compared with the left side (2.60 ms). The authors hypothesized that the PN interval is determined by the interval between the moments when the droplet contacted UpSE and LoSE, termed the UL interval hereafter. Electron transfer occurs from UpSE to ITOE upon the droplet reaching UpSE, leading to a positive output. Conversely, when the droplet contacts LoSE, the charge transfer is reversed, resulting in a negative output. A more detailed discussion on charge transfer will follow later.

To test this hypothesis, the droplet impinging process was analyzed by high-speed imaging (Figure S3). The moment the droplet contacted UpSE was defined as $t = 0$ s. It was observed that the droplet impinging on the right side exhibited a shorter UL interval (1.43 ms) compared with the droplet impinging on the left side (2.86 ms), consistent with the shorter PN interval for the right-side condition. This observation validated the correlation between the PN interval (electric output) and the UL

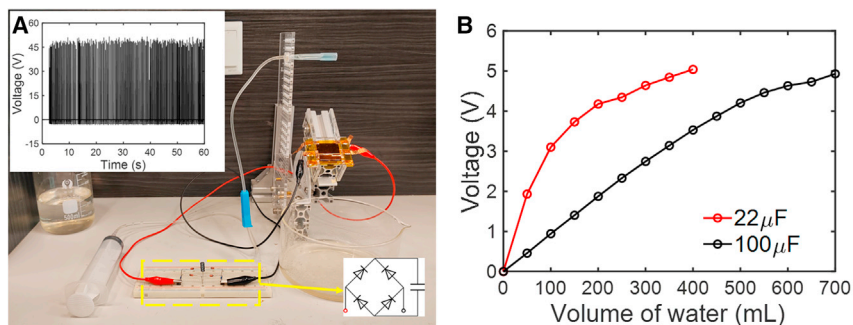


Figure 5. The dropping droplets charge the capacitance

(A) Schematic of charging capacitor. Inset shows the open-circuit voltage before charging.
(B) The voltage of the capacitor when charging.

interval (droplet motion). Notably, there was difference between the PN interval (2.60 ms) and the UL interval (2.86 ms) of the left-side condition, as well as between the PN interval (1.05 ms) and the UL interval (1.43 ms) of the right-side condition. These discrepancies were attributed to the limited sampling interval of the high-speed camera, which was 0.71 ms.

From Figure 4, it can be observed that current decays much faster than the voltage under the same mode. This can be understood from following considerations. The time constant of a circuit is proportional to the resistance.⁴⁹ When measuring the short-circuit current, the resistance is very small, which leads to a short discharge time. The current decays fast. When measuring the open-circuit voltage, the resistance is very high, which leads to a long discharge time.

Here, as many as possible motion states of the droplets are presented. For the UI* mode, the ITO film electrode and UpSE are connected. For the UC* mode, the Cu film electrode and UpSE are connected. According to the shape of the output current and voltage, the FED-TENG working in the two modes is similar to the reported two-electrode droplet-TENG. From Figure S5, it can be seen that the outputs have little difference. When FED-TENG works in LI* and LC* modes, it is also equivalent to the TENG with two electrodes, and the motion state is just that the droplet only comes into contact with the LoSE. The electric output of UI*-LC is linked to the length and arrangement of the two strip electrodes. However, the waveform of the output remains consistent as long as the droplet can contact the two strip electrodes. Apart from UI-LC* and UC-LI*, the electric outputs of other modes are not significantly affected by the two droplet-impinging positions. Subsequent study will focus on the left position.

The FED-TENG has potential applications in harvesting energy from raindrops. While a rain collector is commonly utilized for this purpose, we experimentally employed an injection syringe instead. As shown in Figure 5A, droplets are extruded one by one from the injection syringe, and the open-circuit voltage in UC* mode is recorded. When the droplet impacts the PTFE surface, the capacitor starts charging. Figure 5B demonstrates that the voltage of the capacitor steadily increases with the total volume of the water droplets. This result substantiates the capability of the FED-TENG to harness energy effectively from raindrops.

Considering a constant capacitance, the voltage directly correlates with the amount of electric charge. The voltage across a 22-μF capacitor should theoretically be

approximately 4.5 times that of a 100- μ F capacitor. However, capacitors usually undergo self-discharge after charging. This phenomenon is more pronounced in small capacitors or those charged with a substantial amount of charge. The measured voltages of the two capacitors do not entirely conform to this scaling law.

In a FED-TENG, the film electrode is isolated by PI, PTFE, and substrate. The strip electrode can be replaced by a new one or some other corrosion-resistant conductive material. After 15 months, the FED-TENG was baked at 120°C for 30 min before being tested. Figure S7 displays the outputs of the LC* mode at two time points: immediately after fabrication and after 15 months of storage. Remarkably, the open-circuit voltage did not decrease after being stored for 15 months, indicating a considerable shelf-life.

Dual outputs

Distinguishing itself from conventional water-TENGs that offer a single output, FED-TENG operating in UI*-LC* or UC*-LI* mode can provide dual output through two output ports. The characterization of dual output was performed by concurrently measuring the electric outputs from two output ports using a digital multimeter (DM) and a high-resistance meter (HRM), respectively. These instruments were interchangeably used for electric output measurement (Figure S8). The singly connected modes, UI* and LC*, demonstrated outputs of around 50 V (Figure 6A, left). Under the UI*-LC* mode, both output ports showed an open-circuit voltage of 25–30 V (Figure 6A, right), approximately half of the voltage produced by the singly connected modes. UI*-LC* evenly distributed the total output between the two output ports, suitable for supplying power to multiple similar loads.

On the other hand, the singly connected modes, UC* and LI*, exhibited open-circuit voltages of approximately 50 and 40 V, respectively (Figure 6B, left). In the case of UC*-LI*, the UC port and the LI port generated open-circuit voltages of about 30 and 10 V, respectively (Figure 6B, right). UC*-LI* distributed the major output to the UC port and the minor output to the LI port, providing uneven dual output. This configuration is ideal for operating as a self-powered sensor system, with the lower output serving as a sensor signal and the higher output available to power ancillary function circuits. As previously demonstrated,⁵⁰ the FED-TENG holds potential as a candidate for monitoring liquid leakages in pipes. Additionally, the FED-TENG could serve as a self-diagnostic energy harvester. When functioning outdoors, the FED-TENG could transmit a signal (the lower output) to the receiver when adequate power is available. Based on the magnitude of the signal, it becomes possible to assess the proper functioning of the energy harvester.

Two distinct dual-output configurations were easily discernible during LED-lighting tests (Figure 6C and 6D). Each pair of output ports was connected to two LEDs arranged in parallel with opposite polarity. The LED connected with its positive terminal to CuE or ITOE was designated as a positive LED (pLED), while the other LED was termed as a negative LED (nLED). A combination of a pLED and an nLED represented an AC load, whereas an individual pLED or nLED signified a DC load. LEDs encircled in blue were consistently connected to ITOE, while those encircled in white were consistently connected to CuE.

Under the UI*-LC* mode, evenly distributed dual output illuminated LEDs connected to both UI and LC ports. In contrast, UC*-LI* exhibited unevenly distributed dual output, lighting only LEDs connected to the high-output UC port and leaving LEDs linked to the low-output LI port unlit. Within UI*-LC*, the UI port lit both

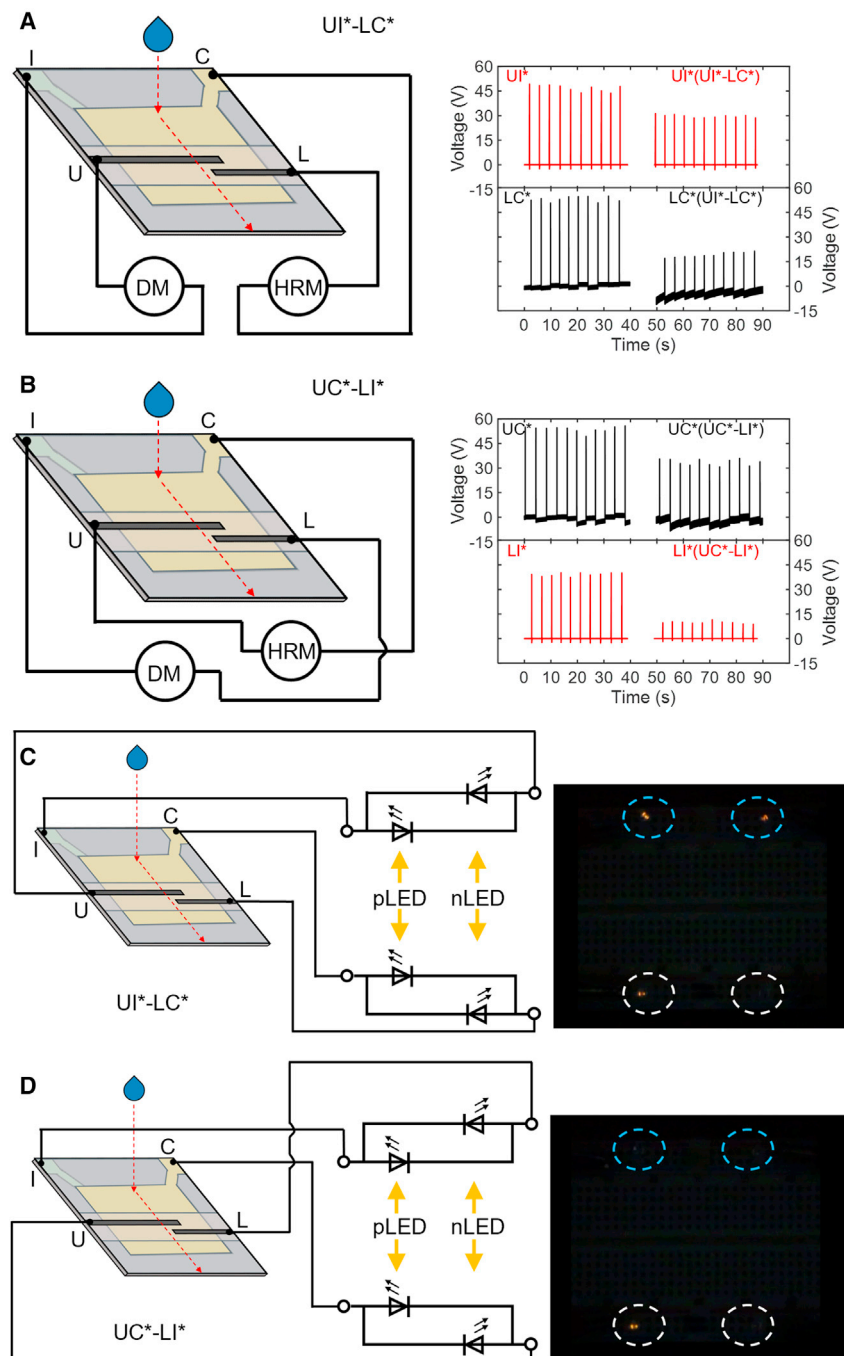


Figure 6. Dual output of FED-TENG

Outputs shown in red line and black line were measured by DM and HRM, respectively.

(A and B) Open-circuit voltage of UI* and LC* (A) and of UC* and LI* (B).

(C and D) Captured image of LED lightening by UI*-LC* (C) and by UC*-LI* (D).

pLED and nLED due to AC output, while the LC port only lit pLED due to DC output (Figure 6C; Videos S1 and S2). Concerning UC*-LI*, the UC port exclusively lit pLED owing to DC output, whereas the LC port did not illuminate any LED due to its low output. Singly connected modes, UI*, LC*, UC*, and LI*, only illuminated pLED due to DC output (Videos S3 and S4).

Mechanism analysis

In the process of liquid-solid contact electrification, both electron transfer and ion transfer occur. The “two-step” model proposed by Wang et al.^{51,52} provides a detailed illustration of this phenomenon. In the first step, when a droplet impinges on the solid surface, water molecules and impurity ions collide with the surface due to the impulsive force from the droplet. As a result of the overlap between the electron clouds of the solid atoms and water molecules, electrons are transferred between them.⁵³ Simultaneously, ionization reactions may also occur on the solid surface.⁵¹ In the second step, electrostatic interactions attract opposite ions in the liquid toward the charged surface, forming an electric double layer (EDL).⁵¹ However, it is likely that electron transfer plays a dominant role in the liquid-solid electrification process.¹⁰

At the outset, the PTFE surface is neutral. Upon impinging, electrons from the droplet are adsorbed onto the PTFE surface,^{10,51,54–56} and these electrons persist even after the droplet departs, with accumulation reaching its saturation point when the surface charge is maximized.²² Friction-induced charge is minimal as the droplet slides off the PTFE surface.^{28,31,57} Interestingly, a large output is observed when the droplet falls from a greater height,⁴⁷ owing to the fixed position of the top electrode, maintaining the droplet’s area upon contacting it. Current and voltage peak values occur when the droplet first contacts the top electrode, while the spreading area continues to increase. It could be concluded that the charge transferred from droplets to the PTFE surface is mainly from impinging. In other words, the impinging will promote the overlap of the electron, making the electrons transfer more easily.

Xu et al.³⁸ demonstrated that the output voltage remains constant regardless of the electrode’s spatial location, indicating that the functional charge exists within a minimal area. As long as the functional-charge area is covered by the droplet, the output remains constant. This charge-concentration area, precisely the impinging area, is challenging to discern and is hypothetically illustrated by the yellow circle in [Figure S9A](#).

Following contact with the PTFE surface, the droplet spreads out due to momentum and gravity, with the upper edge initially rising and then descending. The highest position attained by the upper edge is indicated by a yellow line in [Figure S9A](#). To optimize output, the charge-concentration area should be above both strip electrodes. When contacting LoSE, this area should intersect the droplet-PTFE interface. Horizontally moving the FED-TENG to alter the impinging position of the droplet would create a set of yellow circles forming a zone enclosed by the red line in [Figure S9B](#), a designated steel-electrode function zone. Though changes in the length of the strip electrodes would alter this zone, the droplet will contact each of two strip electrodes in sequence. The two tested impinging positions lie inside this zone, hence yielding similar outputs.

The adsorbed electrons on the PTFE surface induce an electric field. Considering the total thickness of the four-layer film (ITO, PI, Cu, and PTFE) is less than 50 μm , the electric field within the film can be considered uniform and perpendicular to the PTFE surface. Electrostatic induction prompts charge redistribution within CuE and ITOE ([Figure S10A](#)). Upon a droplet’s impingement on the PTFE surface, the cations within the droplet are attracted by the electrons on the PTFE surface, creating an EDL. The presence of these cations screens the electrons on the PTFE surface, thereby partially mitigating the electric field imposed on ITOE and CuE

(Figure S10B). Consequently, induced charges within these electrodes are partially neutralized.

Subsequently, when the droplet slides off, the electric field is restored, causing the induced charges within the electrodes to return. However, the electrostatic induction within ITOE and CuE has minimal impact on the electric output. This deduction is further supported by the test results of the single-electrode model of this FED-TENG, illustrated in Figure S11. The tests show significant outputs between UpSE or LoSE and the ground in the test (Figures S11A–S11D). In contrast, the open-circuit voltage and short-circuit current between ITOE and ground are negligible and overwhelmed by noise (Figures S11E and S11F). Similarly, the voltage and current between CuE and the ground are also minimal (Figures S11G and S11H). These findings affirm the limited charge transfer between ITOE or CuE and the ground.

The electric output results from electron transfer between strip electrodes and film electrodes, where the electron source is the strip electrodes. This analysis starts with the examination of UI*-LC*, serving as a representative example applicable to the analysis of other modes later on. Figures 7 and 8 present a lateral view, vertical view, and an equivalent circuit of FED-TENG for different stages of droplet motion. When the droplet contacts UpSE, the anions in the droplet repel the electrons of UpSE toward the ITOE electrode, thereby generating a positive current ($+I_{UI}$) (Figure 7A). The charge transfer between strip and film electrode is indicated by red positive and negative signs in lateral and vertical views. This process resembles the charging of the capacitor C_{UI} by the EDL. The maximum charging current of $+I_{UI}$ can be estimated using U_{EDL}/R , where U_{EDL} represents the EDL voltage and R symbolizes the resistance of wires and measurement meter (refer to equivalent circuit analysis in the Supplemental information).

Subsequently, when the droplet contacts LoSE, the anions in the droplet drive the electrons of LoSE toward CuE, creating a positive current ($+I_{LC}$) (Figure 7B). This process is proposed as EDL and C_{UI} charging the capacitor C_{LC} . During the charging of C_{LC} by C_{UI} , the charges of C_{UI} diminish, generating a negative discharging current ($-I_{UI}$). As C_{LC} is charged by both EDL and C_{UI} , the charging current ($+I_{LC}$) of C_{LC} results from the discharging currents from both EDL ($-I_{EDL}$) and C_{UI} ($-I_{UI}$). It is anticipated that $+I_{LC} > -I_{UI}$ (where + and - indicate only the current polarity, not the value's sign), a confirmation obtained through electric output measurements (Figures 4A and 4E). It is noteworthy that $-I_{UI}$ contributes significantly to $+I_{LC}$. Therefore, for simplicity, this process can be approximated by C_{UI} charging C_{LC} . The maximum discharging current of $-I_{UI}$ (or charging current $+I_{LC}$) is estimated using $Q/(R \cdot C_{UI})$, where Q represents the sum of charges induced in C_{UI} and C_{LC} (refer to equivalent circuit analysis in supporting Information).

As the droplet continues to slide, the overlapping area between the droplet and the charge-concentration area diminishes, reducing the charging capacity of the EDL. Consequently, both C_{UI} and C_{LC} discharge to the EDL, leading to negative discharging currents ($-I_{UI}$ and $-I_{LC}$) (Figure 7C). It is important to note that these discharging currents are minimal due to the relatively slow change of EDL and the quasi-equilibrium state of capacitors C_{UI} and C_{LC} , and the EDL. C_{UI} and C_{LC} continue to discharge until the droplet leaves UpSE and LoSE. The electron-transfer process of UC*-LI* is delineated in Figure 8.

The difference in output polarity between UI*-LC and other modes (Figure 3) can be elucidated by analyzing the discharging process of the measured ports. In

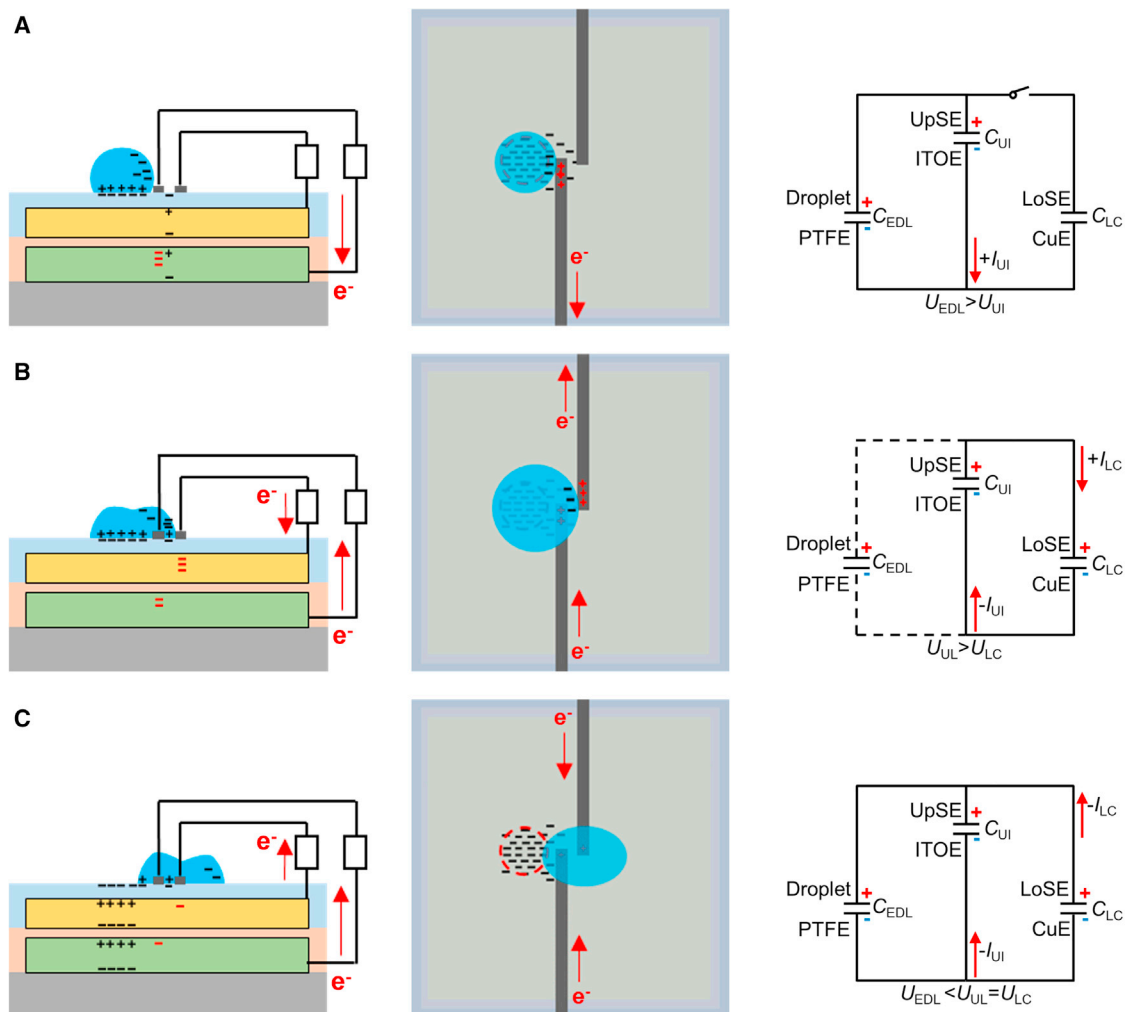


Figure 7. Schematic mechanism and equivalent circuits of FED-TENG for UI*-LC*

Droplet contacts UpSE (A), contacts LoSE (B), and continues to slide on UpSE and LoSE (C).

Legend: glass; ITO; PI; Cu; PTFE; steel; droplet. +, positive charge; -, negative charge; e^- , electron.

UI*-LC, during discharging, the capacitor C_{UI} charges the capacitor C_{LC} (Figure 7B). The maximum discharging current of $-I_{UI}$ is estimated by $Q/(R \cdot C_{UI})$. Similarly, for UC*-LI, during discharging, the capacitor C_{UC} charges the capacitor C_{LI} (Figure 8B), with the maximum discharging current $-I_{UC}$ estimated by $Q/(R \cdot C_{UC})$. Notably, the capacitance of C_{UC} is significantly larger than that of C_{UI} due to the smaller distance between UpSE and CuE compared with that between UpSE and ITOE. Consequently, the discharging current $-I_{UC}$ is significantly smaller than $-I_{UI}$. In practice, $-I_{UC}$ was negligible (Figure S5I), whereas $-I_{UI}$ was noticeably large (Figure 4E).

For other parallelly connected modes (UI-LC* and UC-LI*), the capacitor of the measured ports (C_{LC} of UI-LC* or C_{LI} of UC-LI*) only discharges to the EDL, without charging the other capacitor (Figures 7C and 8C). Since the discharge process to the EDL is a gradual process, the discharging current remains small. In the case of singly connected modes (UI*, LC*, LI*, and UC*), the capacitor of the measured ports solely discharges to the EDL, resulting in a relatively minor discharging current.

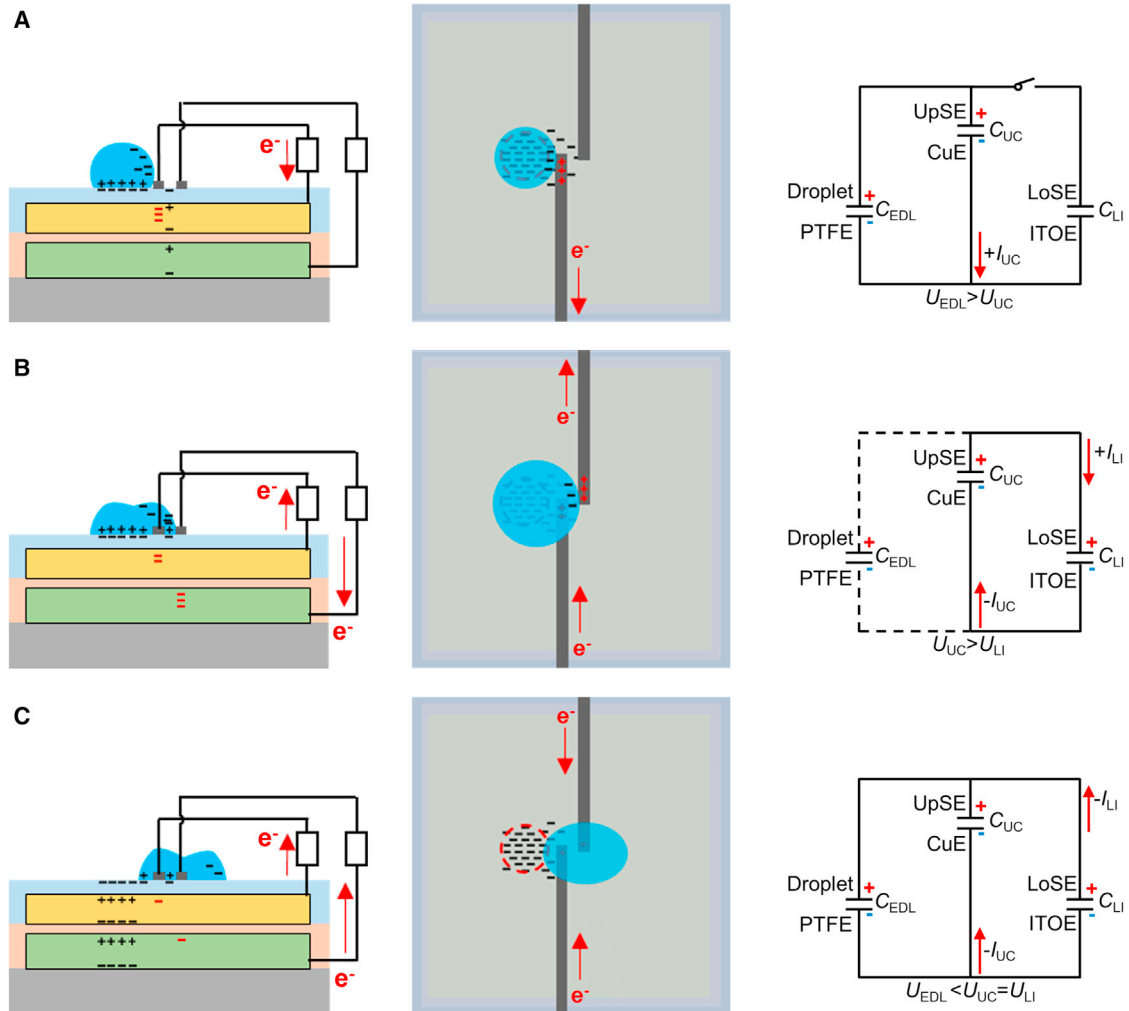


Figure 8. Schematic mechanism and equivalent circuits of FED-TENG for UC*-LI*

Droplet contacts UpSE (A), contacts LoSE (B), and continues to slide on UpSE and LoSE (C).

Legend: glass; ITO; PI; Cu; PTFE; steel; droplet. +, positive charge; -, negative charge; e^- , electron.

In summary, only UI*-LC generates a significant discharging current, thereby leading to the AC electric output.

The divergence in output between UI*-LC* and UC*-LI* (Figure 6) can be traced to the capacitors formed by the film electrode (ITOE or CuE) and the strip electrode (UpSE or LoSE). When the droplet contacts UpSE, the EDL charges the capacitor C_{UI} in UI*-LC* (Figure 7A) (or C_{UC} in UC*-LI* [Figure 8A]). The maximum charging current is estimated by U_{EDL}/R , which remains unaffected by the capacitance. Therefore, $+I_{UI} \approx +I_{UC}$. When the droplet contacts LoSE, the EDL charges C_{LC} in UI*-LC* (Figure 7B) (or C_{LI} in UC*-LI* [Figure 8B]). The maximum charging current is estimated by $Q/(R \cdot C_{UI})$ (or $Q/(R \cdot C_{UC})$). Considering the distance between UpSE and ITOE being larger than that between UpSE and CuE, the capacitance of C_{UI} is smaller than that of C_{UC} . Thus, $+I_{LC} > +I_{LI}$. As $U_{EDL} > Q/C_{UI} > Q/C_{UC}$, $+I_{UI} \approx +I_{UC} > +I_{LC} > +I_{LI}$. Given the output voltage generally aligns with the output current, it is inferred that $U_{UI} \approx U_{UC} > U_{LC} > U_{LI}$, which concurs with measurement results (Figure 6).

In this research, a multimodal FED-TENG was introduced, offering an array of output modes compared with the existing water-TENG. This advancement broadens the spectrum of potential applications. The FED-TENG allows selective generation of DC or AC output, directly accommodating various types of loads. Moreover, it facilitates the production of even or uneven parallel power output, as exemplified through LED demonstrations. Even parallel power output is suitable for supplying power to multiple similar loads, while uneven parallel power output could serve as a self-powered sensor system. In this system, the lower power output functions as a sensor signal, while the higher power output could be stored for auxiliary circuits. The study of FED-TENG is expected to offer crucial insights for enhancing the flexibility and adaptability of water-TENGs, catering to diverse practical applications such as energy scavenging and environment monitoring of rain, rivers, and oceans.

EXPERIMENTAL PROCEDURES

Resource availability

Lead contact

Further information and requests for resources should be directed to, and will be fulfilled by, the lead contact, Wen-Quan Tao (wqtao@mail.xjtu.edu.cn).

Materials availability

This study did not generate new unique reagents.

Data and code availability

Any additional information required to reanalyze the data reported in this article is available from the lead contact upon request.

Fabrication of the FED-TENG

After cleaning the ITO glass (measuring 40 × 40 × 1.1 mm, with a 260-nm ITO thickness) using acetone and ethanol in an ultrasonicator for 5 min, it was dried with compressed air and then baked at 150°C for 5 min. Next, photoresist AZ5214 (Clariant) was spin coated onto the ITO glass at 4,000 rpm for 40 s and baked at 110°C for 90 s. Following this, the glass was covered by a mask and exposed to UV light at a dose of 140 mJ cm⁻². The glass was then immersed in developer NMD-3 until the exposed photoresist was removed. After rinsing, the marginal ITO (5-mm width) was etched off using aqua regia (HNO₃:HCl:H₂O = 1:3:6). Subsequently, a 50-mm-wide and 40-μm-thick piece of PI tape was applied onto the ITO glass. A 200-nm-thick layer of Cu film was evaporated onto the PI tape. Another piece of PI tape, 10-mm wide and 40-μm thick, was applied onto the Cu film. Following this, two steel strips (1.5-mm width and 50-μm thickness) were placed onto the PI tape. The top surface except for the two steel strips (the glass was at the bottom) was covered by dripping 0.5 mL 2 wt % Teflon AF1600X (DuPont) dispersed in FC-40 (3M). The device was placed horizontally in a chemical hood for 5 h to allow the solvent to evaporate completely. Finally, the device underwent subsequent baking on a hotplate at 60°C, 90°C, and 120°C (5 min each), followed by baking at 150°C for 30 min.

Measurement

The detailed droplet impinging process in [Figures S3](#) and [S9](#) was captured by high-speed imaging equipment (Phantom, Micro R111). Contact-angle measurements were conducted using a contact-angle meter (Attension, Theta T200). The surface morphology of the PTFE was observed through a probe-type profilometer (Bruker, Contour GT-K). Output current or voltage was measured using a DM (National

Instruments, PXI-4072) equipped with a terminal block (TB-2606) and a multiplexer switch module (PXI-2503) or an HRM (Keithley 6517B). When measuring current, the internal resistances of DM and HRM were 0 M Ω . For voltage measurements, the internal resistances of DM and HRM were 2 M Ω and infinitely large, respectively. Charge measurements were performed using the HRM. Throughout the experiment, the relative humidity and the environmental temperature were maintained at $62.0\% \pm 5.0\%$ and $29.0\% \pm 2.0\text{ }^{\circ}\text{C}$, respectively. The experiments were conducted in the MEMS laboratory of the Thermo-Fluid Science and Engineering Department of Xi'an Jiaotong University, in which the required room relative humidity and temperature can be maintained by accurate air conditioning and humidifying equipment.

SUPPLEMENTAL INFORMATION

Supplemental information can be found online at <https://doi.org/10.1016/j.xcrp.2024.101800>.

ACKNOWLEDGMENTS

This work was supported by the Foundation for Innovative Research Groups of the National Natural Science Foundation of China (no. 51721004).

AUTHOR CONTRIBUTIONS

Conceptualization, P.H., J.D., and W.-Q.T.; investigation, P.H. and J.D.; methodology, P.H. and J.D.; visualization, P.H. and L.L.; writing – original draft, P.H.; software, J.D.; writing – review & editing, L.L., J.D., and W.-Q.T.; resources, W.-Q.T.; funding acquisition, W.-Q.T.; supervision, W.-Q.T. P.H. and J.D. contributed equally to this work.

DECLARATION OF INTERESTS

The authors declare no competing interests.

Received: August 22, 2023

Revised: November 28, 2023

Accepted: January 10, 2024

Published: January 31, 2024

REFERENCES

- Li, L., Li, X., Yu, X., Shen, C., Wang, X., Li, B., Li, J., Wang, L., Yin, J., and Guo, W. (2022). Boosting the output of bottom-electrode droplets energy harvester by a branched electrode. *Nano Energy* 95, 107024.
- Sun, W., Ding, Z., Qin, Z., Chu, F., and Han, Q. (2020). Wind energy harvesting based on fluttering double-flag type triboelectric nanogenerators. *Nano Energy* 70, 104526.
- Chen, S., Liu, D., Zhou, L., Li, S., Zhao, Z., Cui, S., Gao, Y., Li, Y., Wang, Z.L., and Wang, J. (2021). Improved output performance of direct-current triboelectric nanogenerator through field enhancing breakdown effect. *Adv. Mater. Technol.* 6, 2100195.
- Cheng, R., Dong, K., Chen, P., Ning, C., Peng, X., Zhang, Y., Liu, D., and Wang, Z.L. (2021). High output direct-current power fabrics based on the air breakdown effect. *Energy Environ. Sci.* 14, 2460–2471.
- Ravichandran, A.N., Depoutot, F., Kharbouche, E., Hamand, M., Ramuz, M., and Blayac, S. (2021). Demonstration of friction-based triboelectric nanogenerator and integration in a power-balanced fully autonomous system. *Nano Energy* 83, 105796.
- Sun, Y., Zheng, F., Wei, X., Shi, Y., Li, R., Wang, B., Wang, L., Wu, Z., and Wang, Z.L. (2022). Pendular-Translational Hybrid Nanogenerator Harvesting Water Wave Energy. *ACS Appl. Mater. Interfaces* 14, 15187–15194.
- Ravichandran, A.N., Depoutot, F., Kharbouche, E., Hamand, M., Ramuz, M., and Blayac, S. (2021). Demonstration of friction-based triboelectric nanogenerator and integration in a power-balanced fully autonomous system. *Nano Energy* 83, 105796.
- Zhang, X., Zheng, Y., Wang, D., Rahman, Z.U., and Zhou, F. (2016). Liquid-solid contact triboelectrification and its use in self-powered nanosensor for detecting organics in water. *Nano Energy* 30, 321–329.
- Lee, J.W., and Hwang, W. (2018). Theoretical study of micro/nano roughness effect on water-solid triboelectrification with experimental approach. *Nano Energy* 52, 315–322.
- Nie, J., Ren, Z., Xu, L., Lin, S., Zhan, F., Chen, X., and Wang, Z.L. (2020). Probing contact-electrification-induced electron and ion transfers at a liquid-solid interface. *Adv. Mater.* 32, 1905696.
- Zhang, L., Li, X., Zhang, Y., Feng, Y., Zhou, F., and Wang, D. (2020). Regulation and influence factors of triboelectricity at the solid-liquid interface. *Nano Energy* 78, 105370.
- Wang, Z., Wan, D., Fang, R., Yuan, Z., Zhuo, K., Wang, T., and Zhang, H. (2022). Water-based triboelectric nanogenerator for wireless energy transmission and self-powered communication

- via a solid-liquid-solid interaction. *Appl. Surf. Sci.* **605**, 154765.
13. Zheng, L., Lin, Z.H., Cheng, G., Wu, W., Wen, X., Lee, S., and Wang, Z.L. (2014). Silicon-based hybrid cell for harvesting solar energy and raindrop electrostatic energy. *Nano Energy* **9**, 291–300.
 14. Lin, Z.H., Cheng, G., Lee, S., Pradel, K.C., and Wang, Z.L. (2014). Harvesting water drop energy by a sequential contact-electrification and electrostatic-induction process. *Adv. Mater.* **26**, 4690–4696.
 15. Liang, Q., Yan, X., Liao, X., and Zhang, Y. (2016). Integrated multi-unit transparent triboelectric nanogenerator harvesting rain power for driving electronics. *Nano Energy* **25**, 18–25.
 16. Xiong, J., Lin, M.F., Wang, J., Gaw, S.L., Parida, K., and Lee, P.S. (2017). Wearable all-fabric-based triboelectric generator for water energy harvesting. *Adv. Energy Mater.* **7**, 1701243.
 17. Choi, D., Kim, D.W., Yoo, D., Cha, K.J., La, M., and Kim, D.S. (2017). Spontaneous occurrence of liquid-solid contact electrification in nature: toward a robust triboelectric nanogenerator inspired by the natural lotus leaf. *Nano Energy* **36**, 250–259.
 18. Jang, S., La, M., Cho, S., Yun, Y., Choi, J.H., Ra, Y., Park, S.J., and Choi, D. (2020). Monocharged electret based liquid-solid interacting triboelectric nanogenerator for its boosted electrical output performance. *Nano Energy* **70**, 104541.
 19. Zhong, W., Xu, L., Zhan, F., Wang, H., Wang, F., and Wang, Z.L. (2020). Dripping channel based liquid triboelectric nanogenerators for energy harvesting and sensing. *ACS Nano* **14**, 10510–10517.
 20. Fuwad, A., Ryu, H., Jeon, T.J., and Kim, S.M. (2022). Hybrid film for liquid-solid contact-based energy harvesting systems. *Int. J. Energy Res.* **46**, 1672–1682.
 21. Zhang, J., Lin, S., Zheng, M., and Wang, Z.L. (2021). Triboelectric nanogenerator as a probe for measuring the charge transfer between liquid and solid surfaces. *ACS Nano* **15**, 14830–14837.
 22. Li, Z., Yang, D., Zhang, Z., Lin, S., Cao, B., Wang, L., Wang, Z.L., and Yin, F. (2022). A droplet-based electricity generator for large-scale raindrop energy harvesting. *Nano Energy* **100**, 107443.
 23. Wang, D., Zhang, D., Tang, M., Zhang, H., Sun, T., Yang, C., Mao, R., Li, K., and Wang, J. (2022). Ethylene chlorotrifluoroethylene/hydrogel-based liquid-solid triboelectric nanogenerator driven self-powered MXene-based sensor system for marine environmental monitoring. *Nano Energy* **100**, 107509.
 24. Xu, X., Li, P., Ding, Y., Xu, W., Liu, S., Zhang, Z., Wang, Z., and Yang, Z. (2022). Droplet energy harvesting panel. *Energy Environ. Sci.* **15**, 2916–2926.
 25. Zeng, Y., Luo, Y., Lu, Y., and Cao, X. (2022). Self-powered rain droplet sensor based on a liquid-solid triboelectric nanogenerator. *Nano Energy* **98**, 107316.
 26. Helseth, L.E., and Guo, X.D. (2016). Fluorinated ethylene propylene thin film for water droplet energy harvesting. *Renew. Energy* **99**, 845–851.
 27. Helseth, L.E., and Guo, X.D. (2016). Hydrophobic polymer covered by a grating electrode for converting the mechanical energy of water droplets into electrical energy. *Smart Mater. Struct.* **25**, 045007.
 28. Kil Yun, B., Soo Kim, H., Joon Ko, Y., Murillo, G., and Hoon Jung, J. (2017). Interdigital electrode based triboelectric nanogenerator for effective energy harvesting from water. *Nano Energy* **36**, 233–240.
 29. Chen, G., Liu, X., Li, S., Dong, M., and Jiang, D. (2018). A droplet energy harvesting and actuation system for self-powered digital microfluidics. *Lab Chip* **18**, 1026–1034.
 30. Helseth, L.E. (2020). A water droplet-powered sensor based on charge transfer to a flow-through front surface electrode. *Nano Energy* **73**, 104809.
 31. Liu, C., Wang, Y., Sun, P., Chi, J., Che, L., Zhou, X., Wang, Z., Yang, W., Dong, L., Wang, G., and Yang, X. (2020). A water droplet motion energy harvester with wafer-level fabrication method. *J. Micromech. Microeng.* **30**, 065006.
 32. Wu, H., Mendel, N., van den Ende, D., Zhou, G., and Mugele, F. (2020). Energy harvesting from drops impacting onto charged surfaces. *Phys. Rev. Lett.* **125**, 078301.
 33. Jang, S., Joung, Y., Kim, H., Cho, S., Ra, Y., Kim, M., Ahn, D., Lin, Z.H., and Choi, D. (2022). Charge transfer accelerating strategy for improving sensitivity of droplet based triboelectric sensors via heterogeneous wettability. *Nano Energy* **97**, 107213.
 34. Dong, J., Xu, C., Zhu, L., Zhao, X., Zhou, H., Liu, H., Xu, G., Wang, G., Zhou, G., Zeng, Q., and Song, Q. (2021). A high voltage direct current droplet-based electricity generator inspired by thunderbolts. *Nano Energy* **90**, 106567.
 35. Neo, R.G., and Khoo, B.C. (2021). Towards a larger scale energy harvesting from falling water droplets with an improved electrode configuration. *Appl. Energy* **285**, 116428.
 36. Liu, S., Xu, W., Yang, J., Liu, S., Meng, Y., Jia, L., Chen, G., Qin, Y., and Li, X. (2022). DC output water droplet energy harvester enhanced by the triboelectric effect. *ACS Appl. Electron. Mater.* **4**, 2851–2858.
 37. Zhang, N., Gu, H., Lu, K., Ye, S., Xu, W., Zheng, H., Song, Y., Liu, C., Jiao, J., Wang, Z., and Zhou, X. (2021). A universal single electrode droplet-based electricity generator (SE-DEG) for water kinetic energy harvesting. *Nano Energy* **82**, 105735.
 38. Xu, W., Zheng, H., Liu, Y., Zhou, X., Zhang, C., Song, Y., Deng, X., Leung, M., Yang, Z., Xu, R.X., et al. (2020). A droplet-based electricity generator with high instantaneous power density. *Nature* **578**, 392–396.
 39. Wang, X., Fang, S., Tan, J., Hu, T., Chu, W., Yin, J., Zhou, J., and Guo, W. (2021). Dynamics for droplet-based electricity generators. *Nano Energy* **80**, 105558.
 40. Wu, H., Mendel, N., van Der Ham, S., Shui, L., Zhou, G., and Mugele, F. (2020). Charge Trapping-Based Electricity Generator (CTEG): an ultrarobust and high efficiency nanogenerator for energy harvesting from water droplets. *Adv. Mater.* **32**, 2001699.
 41. Gu, H., Zhang, N., Zhou, Z., Ye, S., Wang, W., Xu, W., Zheng, H., Song, Y., Jiao, J., Wang, Z., and Zhou, X. (2021). A bulk effect liquid-solid generator with 3D electrodes for wave energy harvesting. *Nano Energy* **87**, 106218.
 42. Yang, G., Wu, H., Li, Y., Wang, D., Song, Y., Zhou, Y., Hao, J., Zi, Y., Wang, Z., and Zhou, G. (2021). Direct ink writing of fluoropolymer/CNT-based superhydrophobic and corrosion-resistant electrodes for droplet energy harvesters and self-powered electronic skins. *Nano Energy* **86**, 106095.
 43. Chen, X., Jiang, C., Song, Y., Shao, B., Wu, Y., Song, Z., Song, T., Wang, Y., and Sun, B. (2022). Integrating hydrovoltaic device with triboelectric nanogenerator to achieve simultaneous energy harvesting from water droplet and vapor. *Nano Energy* **100**, 107495.
 44. Helseth, L.E. (2022). Harvesting electrical energy from water drops falling on a vibrating cantilever. *Smart Mater. Struct.* **31**, 035031.
 45. Zheng, Y., Liu, T., Wu, J., Xu, T., Wang, X., Han, X., Cui, H., Xu, X., Pan, C., and Li, X. (2022). Energy conversion analysis of multilayered triboelectric nanogenerators for synergistic rain and solar energy harvesting. *Adv. Mater.* **34**, 2202238.
 46. Xu, X., Wang, Y., Li, P., Xu, W., Wei, L., Wang, Z., and Yang, Z. (2021). A leaf-mimic rain energy harvester by liquid-solid contact electrification and piezoelectricity. *Nano Energy* **90**, 106573.
 47. Zhang, Q., Li, Y., Cai, H., Yao, M., Zhang, H., Guo, L., Lv, Z., Li, M., Lu, X., Ren, C., et al. (2021). A single-droplet electricity generator achieves an ultrahigh output over 100 V without pre-charging. *Adv. Mater.* **33**, 2105761.
 48. Wang, S., Wang, Y., Liu, D., Zhang, Z., Li, W., Liu, C., Du, T., Xiao, X., Song, L., Pang, H., and Xu, M. (2021). A robust and self-powered tilt sensor based on annular liquid-solid interfacing triboelectric nanogenerator for ship attitude sensing. *Sensor Actuator Phys.* **317**, 112459.
 49. Zhang, N., Zhang, H., Xu, W., Gu, H., Ye, S., Zheng, H., Song, Y., Wang, Z., and Zhou, X. (2022). A droplet-based electricity generator with ultrahigh instantaneous output and short charging time. *Droplet* **1**, 56–64.
 50. Zhang, W., Wang, P., Sun, K., Wang, C., and Diao, D. (2019). Intelligently detecting and identifying liquids leakage combining triboelectric nanogenerator based self-powered sensor with machine learning. *Nano Energy* **56**, 277–285.
 51. Lin, S., Xu, L., Chi Wang, A., and Wang, Z.L. (2020). Quantifying electron-transfer in liquid-solid contact electrification and the formation of electric double-layer. *Nat. Commun.* **11**, 399.
 52. Wang, Z.L., and Wang, A.C. (2019). On the origin of contact-electrification. *Mater. Today* **30**, 34–51.

53. Xu, C., Zi, Y., Wang, A.C., Zou, H., Dai, Y., He, X., Wang, P., Wang, Y.C., Feng, P., Li, D., and Wang, Z.L. (2018). On the electron-transfer mechanism in the contact-electrification effect. *Adv. Mater.* *30*, 1706790.
54. You, J., Shao, J., He, Y., Yun, F.F., See, K.W., Wang, Z.L., and Wang, X. (2021). High-electrification performance and mechanism of a water-solid mode triboelectric nanogenerator. *ACS Nano* *15*, 8706–8714.
55. Lin, S., Zheng, M., and Wang, Z.L. (2021). Detecting the liquid-solid contact electrification charges in a liquid environment. *J. Phys. Chem. C* *125*, 14098–14104.
56. Lin, S., Chen, X., and Wang, Z.L. (2022). Contact electrification at the liquid-solid interface. *Chem. Rev.* *122*, 5209–5232.
57. Zhang, J., Lin, S., and Wang, Z.L. (2023). Triboelectric Nanogenerator Array as a Probe for In Situ Dynamic Mapping of Interface Charge Transfer at a Liquid-Solid Contacting. *ACS Nano* *17*, 1646–1652.